



**HAL**  
open science

# High efficiency photocatalytic degradation of Ambroxol over Mn doped TiO<sub>2</sub>: Experimental designs, identification of transformation products, mineralization and mechanism

Asma Tab, Mohamed Dahmane, Chemseddin Belabed, Bachir Bellal, Claire Richard, Mohamed Trari

## ► To cite this version:

Asma Tab, Mohamed Dahmane, Chemseddin Belabed, Bachir Bellal, Claire Richard, et al.. High efficiency photocatalytic degradation of Ambroxol over Mn doped TiO<sub>2</sub>: Experimental designs, identification of transformation products, mineralization and mechanism. *Science of the Total Environment*, 2021, 780, pp.146451. 10.1016/j.scitotenv.2021.146451 . hal-03265721

**HAL Id: hal-03265721**

**<https://hal.science/hal-03265721>**

Submitted on 21 Jun 2021

**HAL** is a multi-disciplinary open access archive for the deposit and dissemination of scientific research documents, whether they are published or not. The documents may come from teaching and research institutions in France or abroad, or from public or private research centers.

L'archive ouverte pluridisciplinaire **HAL**, est destinée au dépôt et à la diffusion de documents scientifiques de niveau recherche, publiés ou non, émanant des établissements d'enseignement et de recherche français ou étrangers, des laboratoires publics ou privés.

1 **High efficiency photocatalytic degradation of Ambroxol over Mn doped TiO<sub>2</sub>:**  
2 **Experimental designs, identification of transformation products,**  
3 **mineralization and mechanism**

4  
5 Asma Tab <sup>a,b</sup>, Mohamed Dahmane <sup>a</sup>, Chemseddin Belabed <sup>c</sup>, Bachir Bellal <sup>d</sup>, Claire  
6 Richard <sup>b\*</sup>, Mohamed Trari <sup>d</sup>  
7

8 (a) Laboratory of Chromatography, Faculty of Chemistry, University of Science and  
9 Technology Houari Boumediène, BP 32 El-Alia, 16111, Algiers, Algeria.

10  
11 (b) Université Clermont Auvergne, CNRS, SIGMA Clermont, ICCF, F-63000,  
12 Clermont-Ferrand, France

13  
14 (c) Laboratory of Materials Physics, Faculty of Physics, University of Science and  
15 Technology Houari Boumediène, BP 32 El-Alia, 16111, Algiers, Algeria.

16  
17 (d) Laboratory of Storage and Valorization of Renewable Energies, Faculty of  
18 Chemistry, University of Science and Technology Houari Boumediène, BP 32 El-  
19 Alia, 16111, Algiers, Algeria.  
20

21 **Abstract**

22 Ambroxol (AMB) is a drug commonly used for chronic bronchitis prevention. Once  
23 released in surface water, this recalcitrant chemical becomes a hazardous pollutant.  
24 Here, we investigated the ability of 1% Mn-doped TiO<sub>2</sub> (Mn-TiO<sub>2</sub>) to mineralize  
25 AMB by photocatalysis. We studied the morphology, and the physical and  
26 electrochemical properties of Mn-TiO<sub>2</sub> using X-ray diffraction, Scanning electron  
27 microscopy, Transmission electron microscopy, X-ray fluorescence, BET method,  
28 UV-visible, and electrochemical study and optimized the AMB degrading  
29 experimental conditions through response surface methodology (RSM). Mn-TiO<sub>2</sub> at  
30 the dose of 0.625 g.L<sup>-1</sup> allowed the complete photodegradation of AMB (30 ppm) at  
31 pH 7 under UVA light irradiation for 30 min while total mineralization in CO<sub>2</sub> (>  
32 96%) was achieved after 24 h of irradiation. Mn-TiO<sub>2</sub> was 1.6-time more efficient  
33 than TiO<sub>2</sub> Degussa P25. Product studies were also carried out by liquid

34 chromatography coupled to electrospray high resolution mass spectrometry. Twenty-  
35 one photodegradation products were detected and identified. In addition, ionic  
36 chromatography analyses revealed the release of  $\text{Br}^-$ ,  $\text{NH}_4^+$ , and  $\text{NO}_3^-$  at respectively  
37 97, 63 and 35% of the total Br, and N initially present in AMB. Finally, the reusability  
38 of the photocatalyst was also tested. After four cycles, the almost complete  
39 photodegradation of AMB was achieved showing that Mn-TiO<sub>2</sub> was highly stable.  
40 This work brings new physical characteristics on Mn-TiO<sub>2</sub> photocatalyst. Moreover, it  
41 is the first study investigating the photocatalytic degradation of recalcitrant AMB  
42 drug.

43

44 **Keywords:** Doped semi-conductor, emerging contaminant, Anti-mucolytic, Response  
45 surface methodology, Photoproducts, Reusability.

46

## 47 **1. Introduction**

48 In recent years, numerous studies have indicated the presence of a new class of  
49 molecules in the aquatic environment, known as "emerging pollutants"(Bagheri et al.,  
50 2021; Salazar et al., 2020a; Tobajas et al., 2017a). The extent of their threat toward  
51 human life, fauna and flora has not yet been completely elucidated, and their recent  
52 detection in water, even at very low amounts (Salazar et al., 2020a), has caused  
53 toxicity to plants, animals and humans (Abbas et al., 2018; Iqbal, 2016), and  
54 represents a new kind of concern that has no regulatory status. The creation of  
55 productive strategies for the degradation of this type of pollutants has become an  
56 urgent question and a subject of high priority for the researchers. (Salazar et al.,  
57 2020b; Tobajas et al., 2017b).

58 Monitoring of these sources has revealed that these pollutants are related to drugs,  
59 pesticides, personal care products, etc. (Yang et al., 2017), which contaminate natural  
60 resources such as urban areas, lakes and rivers. Additionally, several pharmaceutical  
61 products are not adsorbed significantly in the subsoil because of their polar nature and  
62 therefore can infiltrate into groundwater. It is one of the main resources that these  
63 pollutants end up in drinking water, which decreases its quality, thus causing  
64 waterborne infections (Sousa et al., 2018).

65 Chronic obstructive pulmonary disease affects approximately 64 million people  
66 worldwide, and mortality rates should increase. Estimates for 2030, published by the  
67 World Health Organization, predict that chronic obstructive pulmonary disease will  
68 become the third leading cause of death worldwide. This inevitably leads to an  
69 increase in the consumption of medications, which in turn increases concern about  
70 their presence in the aquatic environment and about their potential adverse effects on  
71 non-target populations. AMB (trans-4-[(2-amino-3,5-dibromobenzyl) amino]  
72 cyclohexanol) is an active ingredient used in the chronic bronchitis prevention (Xu et  
73 al., 2015); for complications, such as bronchopulmonary diseases in new borns,  
74 hyaline membrane diseases and in antioxidant therapies. Various analytical techniques  
75 have been reported for AMB titration in both biological and pharmaceutical samples  
76 using liquid chromatography , gas chromatography (Yang et al., 2021),  
77 chromatography with amperometric detection (Erady et al., 2019), UV  
78 spectrophotometry (Yang et al., 2021) and voltammetry (Zhu et al., 2021). In contrast,  
79 little is known regarding its environmental behavior, its degradation (Brüggemann et  
80 al., 2003), interaction with other environmental media and extraction method from  
81 wastewaters (Beckers et al., 2018; Brüggemann et al., 2003; Zhang et al., 2020).  
82 AMB is a biologically recalcitrant substance that for the most part is not degradable in

83 wastewater treatment plants (Zhang et al., 2020). Due to its persistence, it is important  
84 to use other treatments to ensure its elimination from water (Beckers et al., 2018).

85         Consequently, the main challenge is to improve processing technologies  
86 towards new methods that are less harmful, durable, cost effective and non-corrosive  
87 to equipment (Bagheri et al., 2021). In this respect, the photocatalysis is an efficient  
88 advanced oxidation process (AOP) which offers different advantages such as n ability  
89 to apply under ambient temperature and pressure, use to treat emerging pollutants and  
90 to achieve their mineralization to the ubiquitous substances like H<sub>2</sub>O and CO<sub>2</sub>(Tab et  
91 al., 2020). In this respect, TiO<sub>2</sub> is extensively used (Belabed et al., 2014) in many  
92 applications, including paints (Fonseca et al., 2021), toothpastes (Liu et al., 2019), UV  
93 protection (Xu et al., 2020), photovoltaics, gas sensors as well as electro- and  
94 photochromism materials (Li et al., 2017). Moreover, TiO<sub>2</sub> is nontoxic, inexpensive,  
95 chemically stable over the entire pH range, and exhibits excellent performance for  
96 removing pollution from both water and air under UV light, which accounts for only  
97 5% of the solar radiation (Carvalho et al., 2019; Güy and Özacar, 2016; Khan et al.,  
98 2020; Yanalak et al., 2020). However, as dopants, transition metals significantly  
99 improve the photocatalytic performance of TiO<sub>2</sub>, limit the recombination of charge  
100 carriers and shift the spectral photoresponse toward the visible region(Gu et al.,  
101 2020). Several dopants, such as Mn (Ahmed, 2016; Prashad Ojha et al., 2020), Fe  
102 (Wang et al., 2009), Ni(Dong et al., 2018), Co (Qian et al., 2019), Cr (Santara et al.,  
103 2016) and V (Rossi et al., 2018), have been attempted. According to a theoretical  
104 study, most 3*d* elements tend to induce surface states within the TiO<sub>2</sub> band gap by  
105 inserting semiconductors with intermediate bands (Das and Makal, 2020). Therefore,  
106 doping is an attractive approach to provide visible light sensitization centres through  
107 the formation of band-gap states. Mn has the highest potential for allowing wide

108 optical absorption in the visible and infrared regions of solar radiation. As a result of  
109 the modification of the optical properties, there is adequate charge carrier mobility  
110 because the intermediate bands due to Mn doping have a significant band bending.  
111 This behavior enables the transmission of visible photons from the valence band (VB)  
112 to the conduction band (CB). To our knowledge, neither the structural, morphological,  
113 optical and electrochemical properties of Mn-TiO<sub>2</sub> nor its application in  
114 photocatalysis have been studied previously.

115 The main target of this paper was to characterize Mn-TiO<sub>2</sub> as a photocatalyst  
116 and to evaluate its performance for the AMB mineralization. This work was the first  
117 detailed investigation of the photocatalytic AMB degradation. Photolysis and  
118 adsorption of AMB were studied and a multivariate analysis was conducted; In  
119 addition, a statistical model was developed in order to simultaneously optimize three  
120 factors namely, the catalyst dose, AMB concentration and pH. Powerful analytical  
121 techniques such as ultra high performance liquid chromatography (UHPLC)-  
122 electrospray ionization (ESI)- high resolution mass spectrometry (HRMS) and ionic  
123 chromatography were used to identify intermediates and propose the mechanism of  
124 degradation as well as the degree of mineralization during photodegradation. The  
125 reusability of Mn-TiO<sub>2</sub> and the mechanism of the photocatalytic degradation were  
126 also investigated.

127

## 128 **2. Experimental**

### 129 **2.1 Materials and reagents**

130 AMB (Fig. 1 and Table 1) was purchased from Pharmalliance Industry (Algiers)  
131 under hydrochloride form and used without any further treatment. Acetonitrile HPLC  
132 grade (CH<sub>3</sub> CN, ≥ 99.9%), sodium dihydrogen phosphate anhydrous (NaH<sub>2</sub> PO<sub>4</sub> ,

133 99.99%), sodium laureth sulfate ( $\text{CH}_3(\text{CH}_2)_{10}\text{CH}_2(\text{OCH}_2\text{CH}_2)_n\text{OSO}_3\text{Na}$ ,  $\geq 99\%$ ) and  
134 formic acid ( $\text{CH}_2\text{O}_2$ , 98-100%) potassium hydroxide (KOH,  $\sim 45\%$  (T)) and  
135 methanesulfonic acid ( $\text{CH}_4\text{O}_3\text{S}$ ,  $\geq 99\%$ ) reagent grade were purchased from Sigma-  
136 Aldrich. All solutions were prepared in purified water using a RIOS 5 reverse osmosis  
137 and synergy (Millipore) device (resistivity  $18\text{ M}\Omega\cdot\text{cm}$ ,  $\text{DOC} < 0.1\text{ mg}\cdot\text{L}^{-1}$ ). Titanium  
138 dioxide powders were obtained from different providers: Eroxide P90 ( $\text{TiO}_2$ ,  $\geq 99.5\%$ )  
139 and Degussa P25 ( $\text{TiO}_2$ ,  $\geq 99.5\%$ ) from Evonik, Hombikat UV100 ( $\text{TiO}_2$ , 99%) from  
140 Sachtleben, anatase ( $\text{TiO}_2$ , 99.7%), rutile ( $\text{TiO}_2$ , 99.5%) and Mn- $\text{TiO}_2$  ( $\text{TiO}_2$ ,  $\geq 97\%$ )  
141 from Sigma-Aldrich. Sodium sulfate anhydrous ( $\text{Na}_2\text{SO}_4$ ,  $\geq 99\%$ ), sulfuric acid  
142 ( $\text{H}_2\text{SO}_4$ , 95.0-98.0%) and sodium hydroxide (NaOH,  $\geq 98\%$ ), all these reagents were of  
143 analytical grade and purchased from Sigma-Aldrich.

## 144 **2.2 Characterization of the Mn- $\text{TiO}_2$ catalyst**

145 The X-ray diffraction (XRD), using a Siemens D5000 diffractometer, was conducted  
146 to confirm the single phase and to evaluate the mean crystal size (D) of the Mn- $\text{TiO}_2$   
147 nanoparticles. The measurements were performed at room temperature with a Cu  $K\alpha$   
148 radiation source ( $\lambda = 0.15406\text{ nm}$ ) operated at 40 kV and an emission current of 30  
149 mA. The crystallites size (D) was evaluated from the broadening ( $\beta$ , rad.) of the  
150 strongest XRD peak (101):

$$151 \quad D = \frac{K\lambda}{\beta \cos\theta} \quad (1)$$

153 where K (= 0.89) is the shape factor and  $\lambda$  the wavelength of the Cu  $K\alpha$  radiation.  
154 Scanning electron microscopy (SEM, Hirox SEM SH-4000MB) and transmission  
155 electron microscopy (TEM, Hitachi H-7650) equipped with an energy dispersive  
156 spectroscopy (EDS) detector were employed to identify the relief and grain  
157 dimensions. In regard to the SEM analysis, the sample (Mn- $\text{TiO}_2$ ) was deposited on a

158 conductive carbon adhesive. For the TEM observation, the powder was dispersed in  
159 deionized water and sonicated for 15 min. Next, 10  $\mu\text{L}$  of the sonicated suspension  
160 was deposited on carbon-formvar copper grids and left to dry overnight at room  
161 temperature.

162 The distribution and average size of Mn-TiO<sub>2</sub> particles were determined using Image I  
163 software, with a total of 100 particles. The corresponding histogram was obtained  
164 with the software Origin 2019. EDS was used for conducting the elemental  
165 percentage analysis. The X-ray fluorescence (XRF) spectroscopy was conducted with  
166 a Panalytical Axios sequential spectrophotometer, and a rhodium tube was fitted as  
167 the source of radiation to achieve complete Mn photocatalyst loading. Pressed pellets  
168 were used to perform the XRF measurements, and the sample included 10 wt.% wax.  
169 The BET method was employed to calculate the specific surface area using an  
170 ASAP2010 Micrometrics instrument and N<sub>2</sub> gas as adsorbent. The UV-visible  
171 spectrum of Mn-TiO<sub>2</sub> was recorded with a Varian Cary 500 spectrophotometer  
172 attached to an integrating sphere. A PGZ301 potentiostat was used for the  
173 electrochemical study, performed in a three-electrode cell containing Na<sub>2</sub>SO<sub>4</sub> solution  
174 ( $10^{-1}$  mol.L<sup>-1</sup>) as support electrolyte with the working electrode (Mn-TiO<sub>2</sub>), an  
175 auxiliary Pt electrode and a saturated calomel electrode (SCE) as the reference. The  
176 intensity-potential J(E) characteristics were plotted at room temperature at a scanning  
177 rate of 10 mV.s<sup>-1</sup>.

### 178 **2.3 Photocatalytic degradation experiments**

179 The experiments were performed under UVA irradiation; the source was provided by  
180 a fluorescent tube (Philips HPK 15 W) emitting in the near UV region (maximum:  
181 365 nm). Mn-TiO<sub>2</sub> powder and 15 mL of AMB solution were introduced in the  
182 cylindrical Pyrex reactor (13.5 cm height and 1.9 cm internal diameter) that was

183 thermoregulated at 25 °C by water circulation in a water jacket to preclude  
184 vaporization. The suspension was agitated in the dark for 2 h to reach adsorption  
185 equilibrium and illuminated under UVA for 30 min. The degradation was studied  
186 under various conditions by varying the pH of the solution, the initial AMB  
187 concentration ( $C_0$ ) and the Mn-TiO<sub>2</sub> dose. H<sub>2</sub>SO<sub>4</sub> and NaOH (0.1 mol.L<sup>-1</sup>) were used  
188 for adjusting the pH. Aliquots were regularly withdrawn, vigorously centrifuged  
189 (3000 rpm, 5 min) and filtered through a 0.45 μm filter (Waters, Millipore) before  
190 analyses.

## 191 **2.4 Analytical determination**

### 192 **2.4.1 HPLC-UV**

193 The concentration of AMB was determined using a Shimadzu 8040 HPLC system  
194 consisting of LC-20AD-XR binary pumps, an SIL-20ACXR autosampler, a SPD-  
195 M30A diode array detector, a DGU-20A3 degasser, a CTO-20AC column furnace, an  
196 FCV-20AH2 and laboratory solutions Shimadzu software. Analytical separation was  
197 performed using a Nucleodur 100-3 C<sub>18</sub> end-capped column (125 mm×4.0 mm, 3 μm  
198 particle size). The mobile phase was a mixture of (A) 50 mmol.L<sup>-1</sup> NaH<sub>2</sub> PO<sub>4</sub> , 5  
199 mmol.L<sup>-1</sup> CH<sub>3</sub>(CH<sub>2</sub>)<sub>10</sub>CH<sub>2</sub>(OCH<sub>2</sub>CH<sub>2</sub>)<sub>n</sub>OSO<sub>3</sub>Na and (B) CH<sub>3</sub> CN. The gradient  
200 program started with 15% B from 0 to 5 min, 38% B from 5 to 10 min and 45% B  
201 from 10 to 17 min at a flow rate of 0.75 mL.min<sup>-1</sup>. The detection wavelength,  
202 injection volume and column oven temperature were 248 nm, 20 μL and 30 °C,  
203 respectively.

### 204 **2.4.2 Ionic Chromatography**

205 A ThermoScientific Dionex ICS-5000 instrument equipped with a conductometer  
206 detector was employed for ion analysis. A Thermo Scientific Dionex Ion Pac AS11  
207 HC (50 mm×4 mm) column and KOH, as eluent, were used to analyze the anions at  
208 0.25 mL.min<sup>-1</sup> and 30 °C. For the NH<sub>4</sub><sup>+</sup> analysis, a Thermo Scientific Dionex Ion Pac  
209 CS16 HC column (50 mm×3 mm) and CH<sub>4</sub>O<sub>3</sub>S as eluent were used at a flow rate of  
210 0.36 mL.min<sup>-1</sup> and 40 °C.

### 211 **2.4.3 UHPLC-ESI-HRMS**

212 HRMS was performed on an Orbitrap Q-Exactive (Thermoscientific) coupled to an  
213 UHPLC instrument Ultimate 3000 RSLC (Thermoscientific). The mass spectrometer  
214 with heated ESI was operated in both positive and negative ESI modes with a spray  
215 voltage of 3 kV for both modes. The column was a Waters analytical column (2.1  
216 mm×100 mm, 1.7 μm particle size) and the column oven temperature was regulated at  
217 30 °C. The aqueous phase (A) was a mixture of 0.1% CH<sub>2</sub> O<sub>2</sub> - CH<sub>3</sub> CN as the  
218 organic phase (B). The separation was realized with a gradient program that consisted  
219 of 5% and 99% of the mobile phase B from 0-7.5 and 7.5-8.5 min, respectively. The  
220 injection volume was 5 μL, and the flow speed was fixed at 0.450 mL.min<sup>-1</sup>. The  
221 system was monitored by the Xcalibur 2.2 Thermo Fisher Scientific software.

### 222 **2.4.4 TOC analysis**

223 A Shimadzu 5050 TOC analyzer was used to monitor the mineralization of AMB. The  
224 percentage of mineralization was calculated using the following equation:

$$225 \text{ Mineralization} = \frac{(OC_0 - OC_t)}{OC_0} \times 100$$

226 (2)

227 where OC<sub>0</sub> is the organic carbon present in the solution at the initial time and OC<sub>t</sub> at  
228 time t. OC is obtained by subtracting the inorganic carbon from the total carbon.

### 229 **2.5 Multivariate experimental design**

230 Based on the method of single factor analysis, preliminary tests were initially  
231 conducted to determine the ranges of the most prominent experimental parameters  
232 influencing the AMB photodegradation. RSM was used to analyze the interactions  
233 among the AMB concentration, Mn-TiO<sub>2</sub> dose and pH during photodegradation and  
234 to study their simultaneous effects. To assess the combined influence of the  
235 independent variables (AMB concentration, Mn-TiO<sub>2</sub> dose and pH) on two responses  
236 using 15 sets of experiments, the Box-Behnken method of experiments was adopted.  
237 The response factor (Y) corresponding to AMB depletion (percent) after irradiation  
238 for 30 min, as shown in Table 2, displays the ranges and levels of the independent  
239 variables.

240 The Box-Behnken design was used because it is very effective and does not have any  
241 point created by the upper and lower limits of the variables at the vertices of the cubic  
242 region. It has been commonly used to optimize different physical, chemical and  
243 biological processes that have used RSM (Zhang Junwei et al., 2010). To obtain the  
244 experimental matrix and to draw the response surface, the JMP8 (Statistical  
245 Discovery™ from SAS) statistical program was used.

246

### 247 **3. Results and discussion**

#### 248 **3.1 Comparison of the photocatalytic activities of Mn-TiO<sub>2</sub> and other** 249 **photocatalysts**

250 The photocatalytic activity of Mn-TiO<sub>2</sub> was compared to that of other TiO<sub>2</sub>  
251 types, namely, P25, UV100, P90, rutile and anatase, by measuring the loss of AMB  
252 against the irradiation time under UVA light (Fig. 2). Mn-TiO<sub>2</sub> exhibits the highest of  
253 photodegradation with an abatement of 99% after 30 min of irradiation, followed by  
254 P25, P90, anatase, UV100 and rutile with 60, 51, 46, 38 and 12% abatement,

255 respectively. The degradation rate was thus 1.65 times faster with Mn-TiO<sub>2</sub> than with  
256 P25 under UVA light. Previous studies on synthesized Mn-TiO<sub>2</sub> photocatalysts  
257 showed photocatalytic activities, two times higher than TiO<sub>2</sub> P25 (Park et al., 2012).  
258 Moreover, Mn-TiO<sub>2</sub> is also photoactive under visible light (Oseghe et al., 2015). This  
259 could be explained by the fact that doping improved the optical and photoelectrical  
260 properties of TiO<sub>2</sub>. Indeed, doping led to a redshift of Mn-TiO<sub>2</sub> absorption toward the  
261 visible region (Oseghe et al., 2015). The high performance of both commercial and  
262 synthesized Mn-TiO<sub>2</sub> (Park et al., 2012) could be explained by the existence of sub-  
263 band-gap states for effective excitation under irradiation by low energy photons, thus  
264 extending the lifetime of charge carriers by providing a longer diffusion length before  
265 the recombination of (e-/h+) pairs (Oseghe et al., 2015). No detailed studies were  
266 carried out for the selected catalyst (Mn-TiO<sub>2</sub>); thus, we conducted several  
267 characterizations to understand its performance.

### 268 **3.2 Mn-TiO<sub>2</sub> characterization**

269 The XRD analysis was used to characterize the crystal structure, and the  
270 corresponding pattern is shown in Fig. S1. According to JCPDS No. 65-5714, the  
271 characteristic peaks at 29.47, 43.18, 44.18, 45.10, 56.41, 63.49, 64.93, 73.6, 74.32,  
272 81.96, 83.89, 88.74, 90.29, 91.32, 97.56, 99.47, 100.17 and 100.82° are assigned to  
273 the anatase-phase TiO<sub>2</sub> (space group I41/amd) correspond to the reflections from  
274 (101), (103), (004), (112), (200), (105), (211), (213), (204), (116), (220), (107), (215),  
275 (301), (008), (303), (224), (312) crystal planes of the tetragonal TiO<sub>2</sub> structure. The  
276 respective measured *d*-spacings are: 3.51, 2.43, 2.37, 2.33, 1.89, 1.70, 1.66, 1.49, 1.48,  
277 1.36, 1.33, 1.28, 1.26, 1.25, 1.19, 1.17, 1.16 and 1.15 Å.

278 On the other hand, the particle size of the catalyst (*D*= 37 nm) was calculated from the  
279 full width at half maximum by using the acquired data from the XRD pattern. The

280 broadening of the peaks suggests a smaller size of Mn-TiO<sub>2</sub> crystals, which is also  
281 confirmed by the SEM and TEM images. The mean particle size correlates well with  
282 the BET and TEM analysis (Table S1) which also evaluate the structural morphology  
283 of nanocatalyst along with determination of size of its particles.

284 The SEM micrographs (Fig. 3a and b) revealed that the particles have nanoscale sizes  
285 and seem spherical in general. To better explore the particle size distribution and to  
286 study the morphology of the photocatalyst, TEM was also performed. Fig. 3c and d  
287 clearly show that Mn-TiO<sub>2</sub> was formed from crystallites with spherical and uniform  
288 forms in agreement with the results obtained for the Mn-TiO<sub>2</sub> nanoparticles (Prashad  
289 Ojha et al., 2020). The nanospheres were homogeneously dispersed with no  
290 segregation phenomenon (Fig. 3c and d). The dark areas of the TEM images could be  
291 explained by the high electron density (Molnárová et al., 2020). The crystallite size  
292 distribution (histogram, Fig. 4a) was plotted from TEM analysis images, and a mean  
293 size of 30 nm was calculated with diameters in the range (25-35 nm) for more than  
294 50% of the particles. Moreover, these acquired results are in good agreement with the  
295 BET analysis. The Energy-dispersive X-ray (EDS) spectrum accompanied by the  
296 relative weight (%) and atomic (%) of elements were studied to assess the elemental  
297 composition of the photocatalyst. Based on the EDS analysis, Table S1 shows the  
298 elemental composition of the catalyst. As presented in Fig. 4b, all elements exist by  
299 their signals, including Ti, O and Mn. The elemental analysis confirmed that 1% Mn  
300 was introduced and revealed that Mn<sup>2+</sup> ions were inserted in the Ti<sup>4+</sup> sub-lattice owing  
301 to their ionic radii, 0.061 and 0.090 nm, respectively. Finally, the difference in the  
302 atomic ratio may be based on the local analysis with the EDS technique.

303 The XRF analysis allowed us to deduce the elemental composition i.e. the mass  
304 concentrations of elements. The XRF analysis provided the total Mn loading on the

305 photocatalyst (Table S2). Both the EDS and XRF analyses clearly show that TiO<sub>2</sub> are  
306 successfully doped by the hetero-valent ion Mn<sup>2+</sup>.

307 According to the supplier, the surface area of Mn-TiO<sub>2</sub> could be > 14 m<sup>2</sup>.g<sup>-1</sup>. From  
308 our BET analysis, it was deduced that the exact specific surface area was 37 m<sup>2</sup>.g<sup>-1</sup>  
309 (Fig. S2), an attractive property for photocatalysis. Comparing this specific surface  
310 area (37 m<sup>2</sup>.g<sup>-1</sup>) to those of other TiO<sub>2</sub> (Table S1), Mn-TiO<sub>2</sub> had the smallest value,  
311 which revealed that it was not the only factor influencing the photoactivity.

312 The diffuse reflectance was used to investigate the optical properties of Mn-TiO<sub>2</sub>. The  
313 diffuse reflectance spectrum is shown in Fig. S3. The band gap value is 2.88 eV (=  $1240/\lambda$ ).  
314 Using the diffuse reflectance data, the gap E<sub>g</sub> (Eq. 3) was obtained with a  
315 direct transition, and its value was reliably determined from the well-known formula:

$$316 (\alpha h \nu)^m = \text{Constant} \times (h\nu - E_g) \quad (3)$$

317 where  $\alpha$  and  $\nu$  are the optical absorption coefficient and the light frequency, the  
318 exponent  $m$  provides information about the transition type. Compared to pure TiO<sub>2</sub>  
319 anatase in the literature, the spectral photoresponse is shifted toward longer  $\lambda$  values.  
320 This result could be due to the appearance of electronic states within the band gap  
321 (sub-band-gap states) explained by the gap decrease due to the quantum effect (H. Y.  
322 Liu et al., 2020). Consequently, the distance of charge transfer between the valence or  
323 conduction band of TiO<sub>2</sub> and Mn-3d electrons is shortened, leading to a visible light  
324 absorption response.

325 To our knowledge, only few papers have reported on the photo-electrochemistry of  
326 Mn-TiO<sub>2</sub> (Ning et al., 2016); thus, an in-depth electrochemical study was undertaken.  
327 The current density-potential J(E) characteristics were plotted in the range of -1 to 1  
328 V<sub>RHE</sub> in Na<sub>2</sub>SO<sub>4</sub> solution (pH ~ 7) at a scan rate of 10 mV.s<sup>-1</sup> to elucidate the

329 interfacial reactions and to delimit the electrochemical stability (Fig. 5a). The  
 330 experiments were performed once the open-circuit potential stabilized. The  
 331 photocurrent ( $J_{ph}$ ) starts to flow at a potential of  $E_{on} \sim 0.01 V_{RHE}$  (Fig. 5a) and  
 332 increases in the anodic direction, indicating the  $n$ -type nature of Mn-TiO<sub>2</sub>. However,  
 333 the recombination of electron/hole ( $e^-/h^+$ ) pairs at the trapping levels and/or grain  
 334 boundaries was evidenced by the lack of current saturation. The capacitance potential  
 335 ( $C^{-2}$ -E) plot (Fig. 5c) provides an accurate flat-band potential of  $E_{fb} = -0.84 V_{RHE}$  and  
 336 an electron concentration  $N_D = 1.9 \pm 0.1 \times 10^{16} \text{ cm}^{-3}$  from the intersection of the  
 337 potential axis at infinite capacity ( $C^{-2} = 0$ ) and the slope of the linear part:

$$338 \quad C^{-2} = \frac{2}{S^2} \frac{e}{\epsilon \epsilon_0} N_D \{E - E_{fb}\} \quad (4)$$

340 where  $\epsilon_0$  is the permittivity of vacuum,  $\epsilon$  ( $= 98$ ) the permittivity of Mn-TiO<sub>2</sub> (B. Liu et  
 341 al., 2013),  $e$  the electron charge and  $S$  the geometric surface area of Mn-TiO<sub>2</sub>. The  $n$ -  
 342 type behavior of Mn-TiO<sub>2</sub> is supported by the positive slope of the ( $C^{-2} - E$ ) plot.

343 In regard to the quantification of the electrical contributions at the Mn-  
 344 TiO<sub>2</sub>/electrolyte interface, electrochemical impedance spectroscopy (EIS) was  
 345 performed. The EIS data of the Mn-TiO<sub>2</sub>/Na<sub>2</sub>SO<sub>4</sub> junction were obtained at the open-  
 346 circuit potential (Fig. 5d). The semicircle at high frequencies is assigned to the bulk  
 347 effect whose center is positioned below the real axis. The depletion angle accounted  
 348 for the non-ideal component of the capacity attributed to the sub-band-gap states and  
 349 rugosity of the electrode, which introduce a constant phase element (CPE):

$$350 \quad Z_{CPE} = \frac{Q^{-1}}{(j\omega)^k} \quad (5)$$

352 where  $Q$  is independent of the frequency,  $j$  the complex number ( $j^2 = -1$ ),  $\omega$  the  
 353 angular frequency, and  $k$  the homogeneity factor ( $0 < k \leq 1$ ). The displacement from

354 the origin is equal to the electrolyte resistance ( $R_{el} = 105 \Omega \cdot \text{cm}^2$ ) due mainly to the  
355 molar conductivity of the most mobile ion  $\text{h}^+$  ( $350 \Omega^{-1} \cdot \text{cm}^2 \cdot \text{mol}^{-1}$ ).

### 356 3.3 Adsorption of AMB on Mn-TiO<sub>2</sub>

357 Fig. S4a shows the amounts of AMB adsorbed per gram of Mn-TiO<sub>2</sub> ( $Q_t$ ) vs.  
358 the contact time, the equilibrium was reached after 2 h of stirring. The adsorption can  
359 be described by the Freundlich model (Eq. 6) (Bekkouche et al., 2012; Ghosh et al.,  
360 2019; Malakootian et al., 2020; Pal et al., 2016)

$$361 \quad Q_e = K_F C_e^{1/n}$$

362 (6)

363 The linearization of Eq. (6) indicates the relationship between  $\ln Q_e$  and  $\ln C_e$  (Eq. 7).

$$364 \quad \ln Q_e = \ln K_F + \frac{1}{n} \ln C_e$$

365 (7)

366 where  $Q_e = (C_o - C_e) \times V/m$  represents the adsorbed quantity of AMB per unit of  
367 mass of Mn-TiO<sub>2</sub> ( $\text{mg} \cdot \text{g}^{-1}$ ),  $C_e$  the AMB concentration at equilibrium ( $\text{mg} \cdot \text{L}^{-1}$ ) and  $K_F$   
368 is the Freundlich coefficient. The coefficient  $n$  is related to the adsorption mechanism.

369 Fig. S4b shows that good linearity is obtained by plotting  $\ln Q_e$  against  $\ln C_e$ . The  
370 constants  $K_F$  and  $1/n$  deduced from the intercept and the slope are listed in Table S3.

371  $K_F$  is equal to 0.54 and  $n = 4.24$ . The value  $1/n < 1$  corresponds to a L-shape that refers  
372 to a decrease in the site availability as the concentration of the drug increases. As

373 shown in Table S3, the adsorption coverage and the adsorption constant of AMB on

374 Mn-TiO<sub>2</sub> are small compared to those of other phenolic derivatives on other TiO<sub>2</sub>

375 photocatalysts (Bekkouche et al., 2012; Pal et al., 2016). This result could be

376 explained by the weak interaction AMB (adsorbate)-Mn-TiO<sub>2</sub> (adsorbent)

377 (Bekkouche et al., 2012; Pal et al., 2016).

### 378 3.4 Kinetics of photocatalytic degradation

379 Fig. S5a compares the loss of AMB vs. time in the absence of Mn-TiO<sub>2</sub>  
380 (photolysis), in the presence of Mn-TiO<sub>2</sub> (adsorption) and in the presence of Mn-TiO<sub>2</sub>  
381 upon irradiation (photocatalysis). While the AMB concentration remains almost  
382 unchanged after 30 min of irradiation (< 3% degradation) in photolysis and decreases  
383 by 10% through the dark adsorption, a complete degradation (> 95%) is achieved by  
384 photocatalysis. For most organic compounds (Arshad et al., 2020; Ghenaatgar et al.,  
385 2019), the photodegradation rate follows a pseudo-first order (Fig. S5b) model and  
386 can be linearized as (8):

$$387 \quad \ln \frac{C_t}{C_0} = -k_{app} \times t$$

388 (8)

389 where  $k_{app}$  (min<sup>-1</sup>) is the apparent first-order rate constant and  $C_t$  and  $C_0$  are the AMB  
390 concentrations at time  $t$  and after dark adsorption, respectively. Fig 10b confirms the  
391 pseudo-first-order kinetics for AMB with a high correlation coefficient  $R^2$  (> 0.995).

### 392 **3.5 Construction of the polynomial expression and 3D response surface**

#### 393 **3.5.1 Statistical analysis**

394 A three-variable Box-Behnken design was used to optimize the AMB  
395 photocatalytic degradation on Mn-TiO<sub>2</sub>. This design was chosen owing to its  
396 productivity and involves only a limited number of experiments. The spherical design  
397 contains all points that lie on a two-square root radius sphere. There are no points on  
398 the vertices of the cubic area generated by the lower and upper limits of every  
399 variable (Ray et al., 2009). The polynomial equation of the empirical second order  
400 was generated for AMB elimination % (Table 2) as the response variable with three  
401 independent variables:

$$\begin{aligned}
402 \quad Y &= 97.92 + 3.10X_1 - 19.55X_2 + 1.23X_3 + 2.99X_1X_2 + 1.26X_1X_3 + 0.47X_2X_3 - \\
403 \quad &3.92X_1^2 - 16.3X_2^2 - 4.24X_3^2 \\
404 \quad &(9)
\end{aligned}$$

405 where Y represents the AMB removal (%) and  $X_1$ ,  $X_2$  and  $X_3$  are the coded values of  
406 the Mn-TiO<sub>2</sub> dose, initial AMB concentration and pH respectively. Using variance  
407 analysis, the experimental data were analyzed for AMB removal from a statistical  
408 point of view. The ANOVA for the responses of the second-order quadratic  
409 polynomial indicated that this model was very significant, as the F-value for the  
410 1044.693 model and the corresponding *p*-value was small (< 0.0001). This result  
411 indicated that, regardless of noise, there is only 0.01% probability of the variable F-  
412 value occurring. The lack of fit should be negligible for this model to be widely used  
413 for producing predictions. The determination of the coefficient was explained as the  
414 ratio of the variation, which showed that the total variation could be used as a  
415 measurement of the model degree of fitting. The expected R<sup>2</sup> value (= 0.998) is in  
416 good agreement with the corresponding modified R<sup>2</sup> value (= 0.996). The R<sup>2</sup> value  
417 must be close to 1 for the best fitting of the experimental results. The smaller the R<sup>2</sup>  
418 value is, the lower the model adaptation to the experimental data. The R<sup>2</sup> values  
419 showed that the quadratic polynomial (Mona et al., 2011) was used to forecast the  
420 experimental degradation of AMB. The AMB removal was plotted against the  
421 corresponding observed values in Fig. S6.

422 In the event of AMB degradation, the independent variables of the quadratic  
423 polynomial  $X_1$  and  $X_2$ , the interaction of the Mn-TiO<sub>2</sub> dose ( $X_1$ )/AMB concentration  
424  $C_0$  ( $X_2$ ),  $X_1X_2$  and the quadratic terms  $X_1^2$ ,  $X_2^2$  and  $X_3^2$  are very significant, as their *p*-  
425 values are smaller than 0.001.

426 From the regression coefficients, the order for which the independent variables  
427 influenced AMB degradation is as follows: initial AMB concentration ( $X_2$ ) > Mn-  
428 TiO<sub>2</sub> dose ( $X_1$ ) > pH ( $X_3$ ). The positive effects of  $X_1$  and  $X_3$  are very low compared to  
429 the negative effect of  $X_2$ , which agree with the reports of the preliminary experiments.  
430 Thus, the AMB concentration ( $C_0$ ) is the dominant factor influencing the AMB  
431 photodegradation on Mn-TiO<sub>2</sub>. This result is found to efficiently generate oxidizing  
432 species such as hydroxyl radicals ( $\bullet$ OH).

### 433 3.3.2 Response surface methodology

434 Using RSM, the effects of independent variables (the Mn-TiO<sub>2</sub> dose, AMB  
435 concentration and pH) and their interaction on AMB degradation were graphically  
436 illustrated by three-dimensional response surface plots and two-dimensional contour  
437 plots. The responses were provided, and the optimal photodegradation percentage was  
438 studied (Zhang Junwei et al., 2010). The interaction effect of the dose of Mn-TiO<sub>2</sub> and  
439 concentration  $C_0$  on the degradation rate is shown in Fig. 6a. which shows that the  
440 degradation percentage of AMB diminished with increasing concentration  $C_0$ . As  
441 shown from the contour diagram (Fig. 6b), a maximal photodegradation was observed  
442 in the concentration range (10 – 30 ppm). The AMB photodegradation increased with  
443 an increasing the Mn-TiO<sub>2</sub> amount until an optimal value of 0.7 g.L<sup>-1</sup>, after which it  
444 remained almost constant, regardless of the dose of the photocatalyst. According to  
445 the contour plots, the maximum photodegradation occurred in the region (0.6 - 1 g.L<sup>-1</sup>).  
446 Fig. 6c shows the influence of the concentration  $C_0$  (AMB) and pH on the  
447 photodegradation kinetics. According to Fig. 6d and as expected, the  
448 photodegradation increased slightly with pH regardless of the concentration of AMB,  
449 and the maximum region occurred in the pH region (6-8). Likewise, the augmentation  
450 in initial AMB concentration indicated a diminution in the photodegradation rate.

451 Moreover, the maximum domain is in the range (10–30 ppm), which is feasible at  
452 higher AMB concentrations. The effects of the pH and Mn-TiO<sub>2</sub> dose on the rate of  
453 AMB removal are shown in Fig. 6e. One can see that the photodegradation rate  
454 slightly increased with increasing pH up to pH 8 and then slowly decreased at high  
455 catalyst doses. From the contour plot (Fig. 6f), the maximum domain was in the range  
456 (0.6 - 0.9 g.L<sup>-1</sup>) of the Mn-TiO<sub>2</sub> dose and pH of 7-8.

### 457 **3.5.3. Optimization of the independent variables and the validation experiment**

458 Any reaction system needs to be optimized using various analytical techniques  
459 and design methodologies to achieve optimal operating conditions and yield the best  
460 result. In this study, efforts have been focused on maximizing the AMB concentration  
461 C<sub>0</sub> to keep the pH as close as possible to a natural pH and to limit the amount of  
462 catalyst used. A Mn-TiO<sub>2</sub> dose of 0.7 g.L<sup>-1</sup>, an AMB concentration of 37.7 ppm and a  
463 pH of 7.7 for the aqueous suspension were found to be optimal for the  
464 photodegradation under the mentioned constraints. According to these conditions, the  
465 RSM predicted the photodegradation rate of AMB of 90%. The results clearly  
466 indicated the efficient utilization of RSM to optimize the photocatalytic degradation  
467 on Mn-TiO<sub>2</sub> (Moztahida and Lee, 2020). Given these conditions, the model provided  
468 a photodegradation abatement of 89%. The results showed the efficiency of the RSM  
469 (Moztahida and Lee, 2020) for determining the optimal parameters of AMB  
470 degradation on Mn-TiO<sub>2</sub> under UVA light.

471 To verify and validate the model accuracy, AMB photodegradation was  
472 performed in batch mode under optimal conditions. From the validation experiments,  
473 the photodegradation reached 89%, a result in perfect accordance with the predicted  
474 results. Consequently, the successful calculation of the optimum point was

475 demonstrated by RSM. This technique could be employed for the optimization of the  
476 photocatalytic degradation of AMB in the presence of Mn-TiO<sub>2</sub>.

### 477 **3.6 Photocatalytic activity of Mn-TiO<sub>2</sub> under optimized conditions**

#### 478 **3.6.1 Involvement of hydroxyl radicals in the reaction**

479         AMB can be oxidized by valence band h<sup>+</sup> or by •OH radicals, a degradation by  
480 poorly oxidant O<sub>2</sub><sup>•-</sup> appearing very unlikely. Indeed, aromatic pollutants are generally  
481 reactive with both species, and the addition of alcohols at moderate concentration is a  
482 way to selectively inhibit the free •OH-mediated processes (Amine-Khoja et al, 2005).  
483 Ethanol (10<sup>-2</sup> - 10<sup>-1</sup> mol.L<sup>-1</sup>) was used to quench these species and added to the  
484 mixture containing AMB and Mn-TiO<sub>2</sub>. Fig S7 shows that ethanol inhibited the  
485 photocatalytic degradation of AMB by 54 % at 10<sup>-2</sup> mol.L<sup>-1</sup> and by 90-95% at 5.10<sup>-2</sup>  
486 mol.L<sup>-1</sup> and above. If we make the hypothesis that until 10<sup>-2</sup> mol.L<sup>-1</sup> ethanol only  
487 scavenged free •OH, then one can conclude that AMB was mainly oxidized by •OH  
488 whereas h<sup>+</sup> only played a secondary role in the reaction. The significant contribution  
489 of •OH to the reaction here using Mn-TiO<sub>2</sub> was previously reported with TiO<sub>2</sub>  
490 Wackherr (Soji et al., 2011). but not observed with TiO<sub>2</sub> Degussa P25 (Soji et al.,  
491 2011). A plausible explanation of this result may come from the different  
492 compositions of the catalysts, as both TiO<sub>2</sub> Wackherr and Mn-TiO<sub>2</sub> crystallizes  
493 exclusively in the anatase variety, whereas TiO<sub>2</sub> Degussa P25 consists of 85% anatase  
494 and 15% rutile (Vione et al., 2005). This may suggest that the presence of the rutile  
495 phase affected the contribution of h<sup>+</sup> in the photocatalytic process. Nevertheless, the  
496 connection between the degradation pathways and crystalline phase needs  
497 supplementary studies.

#### 498 **3.6.2 Photoproducts studies**

##### 499 **3.6.2.1 Identification of the AMB transformation products (TPs)**

500 One of the goals in this work was to optimize the photocatalytic degradation of  
501 AMB based on the kinetic parameters, but the identification of TPs was also of high  
502 importance because in some cases, the degradation products are more hazardous than  
503 the parent compound (Bansal and Sud, 2013). To consider this issue, UHPLC-HRMS  
504 analyses were carried out. Solutions withdrawn after 10 min (30% of AMB  
505 conversion), 30 min (95% of AMB conversion) and 4 h of irradiation were analyzed  
506 and 21 TPs were detected, as listed in Table S4. Table S4 indicates in which ESI  
507 mode, positive or negative, the TPs were detected, along with the experimental and  
508 theoretical  $m/z$  values of the detected ions, error in ppm, chemical formula of the  
509 neutral TP and possible structure. The tolerance error value of  $m/z$  was 5 ppm.

510 AMB had a molecular ion cluster of  $m/z = 376.9860/378.9825/380.9800$  with  
511 an isotope distribution of 1:2:1, in accordance with the two isotopes of Br (78.9178  
512 and 80.9157) with natural abundances of 50.5 and 49.5%. TP1, TP2 and TP3 showed  
513 the same three ion clusters with  $m/z = 392.9788/ 394.9782/ 396.9762$ ,  $m/z = 377.9620/$   
514  $379.9658/ 381.9598$  and  $m/z = 263.8754/ 265.8644/ 267.8629$ , respectively. These  
515 samples had therefore kept the two Br atoms. TP1 gained one O atom compared to  
516 AMB, while in TP2,  $\text{NH}_2$  was replaced by OH, and TP3 was formed following  
517 cleavage of the aliphatic substituent. Given their two ion clusters with  $m/z =$   
518  $315.0689/ 317.0669$  and  $m/z = 313.0542/ 315.0520$ , and their isotope distribution of  
519 1:1, TP4 and TP5 were identified as monobrominated derivatives. Based on the  
520 probable chemical formulas  $\text{C}_{13}\text{H}_{19}\text{O}_2\text{N}_2\text{Br}$  and  $\text{C}_{13}\text{H}_{17}\text{O}_2\text{N}_2\text{Br}$ , one could conclude  
521 that TP4 was generated after the loss of Br and the gain of OH and TP5 after the loss  
522 of Br and 2 H atoms and the gain of OH. The other TPs detected were all  
523 debrominated. TP6 with  $m/z = 267.1335$  corresponded to  $\text{C}_{13}\text{H}_{18}\text{O}_4\text{N}_2$ , which

524 indicates the replacement of two Br atoms by two OH groups and the addition of one  
525 O atom.

526 Photoproducts TP7 to TP12 showed  $m/z$  values between 186.1126 and  
527 114.0913 and contained between 9 and 6 C atoms and 11 to 17 H atoms; thus, these  
528 TPs could be assigned to aminocyclohexanol ( $C_6H_{11}ON$ ) derivatives formed  
529 following the detachment of the aromatic ring. TP11 might correspond to  
530 aminocyclohexanol, and TP12 to aminocyclohexanone. With  $C_9H_{17}O_3N$ ,  $C_8H_{15}O_3N$   
531 and  $C_7H_{13}O_3N$ , TP7, TP8 and TP9 differed by  $CH_2$  and could be assigned to  
532 aminocyclohexanols with  $-(CH_2)_2-CO_2H$ ,  $-CH_2-CO_2H$  and  $CO_2H$  substituents on NH.  
533 TP13 and TP14 with  $m/z = 134.1174$  and  $128.0340$  likely had chemical formulas of  
534  $C_6H_{15}NO_2$  and  $C_5H_7NO_3$  and were formed by opening the cyclohexane ring. The other  
535 TPs with  $m/z$  ranging from  $128.0340$  to  $59.0127$  contained between 6 and 2 C atoms  
536 and corresponded to small molecules often detected after photodegradation of  
537 aromatic compounds (Y. Liu et al., 2013).

538 For comparison, UHPLC-HRMS analyses of AMB irradiated in the presence  
539 of  $TiO_2$  Degussa P25 were carried out. They were also carried out at two conversion  
540 extents: 30 and 95%. TP1-TP14 were detected as for Mn- $TiO_2$ , and two new  
541 degradation products were detected in  $ESI^+$ . With  $m/z = 374.9702$ ,  $376.9682$ ,  
542  $378.9661$  and  $m/z = 372.9544$ ,  $374.9522$ ,  $376.9501$ , these compounds correspond to  
543  $C_{13}H_{16}ON_2Br_2$  and  $C_{13}H_{14}ON_2Br_2$  for the neutral molecules and thus to the  
544 elimination of 2 and 4 H atoms respectively.

545

### 546 **3.6.2.2 Mineralization process**

547  $CO_2$  results from the ultimate photodegradation of organic compounds in  
548 photocatalysis, and its monitoring provides information about the real efficiency of

549 the photocatalytic process. The profile of CO<sub>2</sub> formation under irradiation is shown  
550 Fig. S8. After 30 min of irradiation corresponding to complete AMB loss,  
551 approximately 5% of the initial organic carbon was converted into CO<sub>2</sub>, meaning that  
552 at this stage, AMB was essentially transformed into intermediary products. Total  
553 mineralization (> 96%) was achieved after 24 h of irradiation. Moreover, AMB  
554 contains two Br atoms and two amino groups; hence, Br<sup>-</sup>, NH<sub>4</sub><sup>+</sup> and/or NO<sub>3</sub><sup>-</sup> ions  
555 might also be generated during degradation (Ganzenko et al., 2020). The formation of  
556 these three ions was monitored by ionic chromatography. Data are presented in Fig.  
557 S8. after 12 h of irradiation. After 12 h of irradiation, at least 97% of the Br atoms  
558 were released in solution as Br<sup>-</sup> and the concentration of NH<sub>4</sub><sup>+</sup> reached a plateau at  
559 63% of the total N initially present in AMB, while the concentration of NO<sub>3</sub><sup>-</sup> was at  
560 15% and increased progressively until 35% at 24 h. Further oxidation of NH<sub>4</sub><sup>+</sup> into  
561 NO<sub>3</sub><sup>-</sup> appeared possible. These data showed that Mn-TiO<sub>2</sub> was efficient as a  
562 photocatalyst in the elimination and full mineralization of AMB.

### 563 **3.6.2.3 Photodegradation mechanism of AMB**

564 The main degradation pathways under Mn-TiO<sub>2</sub> are summarized in Scheme 1.  
565 Based on the TP structures, it can be supposed that the attack of AMB by •OH  
566 initially led to the replacement of Br by OH (Xu et al., 2011) and of NH<sub>2</sub> by OH (Li et  
567 al., 2019), along with the oxidation of the aromatic ring or cyclohexanol ring and the  
568 cleavage of the C-C bond linking the aromatic to the aliphatic chain. The presence of  
569 three C atoms linked to N in TP7 showed that one of the C atoms came from the  
570 aromatic ring. TP7 was thus generated by cleavage of the aromatic ring. Further  
571 oxidations induced the cleavage of the aromatic and cyclohexanol rings to form small  
572 carboxylic acids and carbonyls before full mineralization.

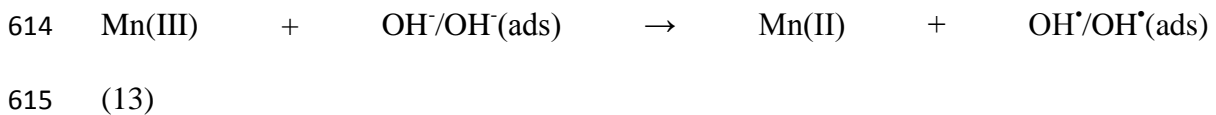
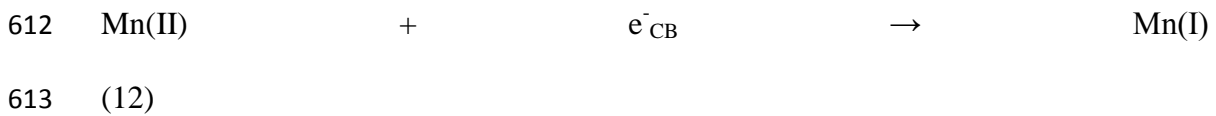
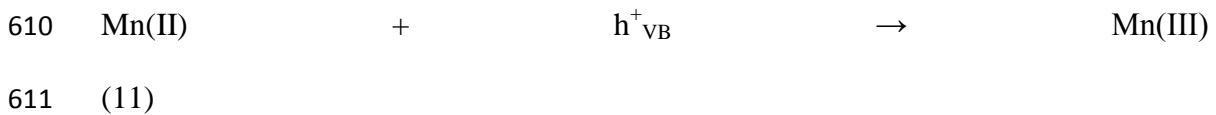
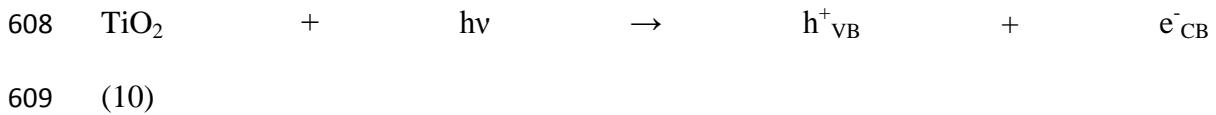
### 573 **3.7 Reusability of the catalyst**

574 From the economic and practical point of view, the recyclability and stability  
575 of the catalyst is one of the main concerns that has a high impact for its application  
576 during the degradation process (Ong et al., 2018). We thus studied the stability of Mn-  
577 TiO<sub>2</sub> by carrying out 4 successive photocatalytic cycles. Between each cycle, the  
578 suspension containing the photocatalyst was centrifuged, collected, thoroughly rinsed  
579 with deionized water and dried at 100 °C for 24 h. Moreover, the structure and  
580 composition of Mn-TiO<sub>2</sub> after reuse were reanalyzed by XRD, TEM and SEM to  
581 check the stability of the oxide. A very good efficiency was obtained even after 4  
582 cycles, with each lasting 30 min. The photodegradation performance was nearly  
583 unchanged with an abatement close to 100% (Fig. 7a). These results imply that the  
584 intermediates were not adsorbed either on the surface or in the pores and channels of  
585 the catalyst. According to the XRD pattern (Fig. 7b), SEM image (Fig. 7c) and TEM  
586 analysis (Fig. 7d), there were no detectable changes in the structure and composition  
587 compared to the analysis performed before photocatalysis. Such results provided clear  
588 proof of the high photocatalytic performance and chemical stability of the used Mn-  
589 TiO<sub>2</sub>.

### 590 **3.8 Mechanism of $\cdot\text{OH}$ formation from the Mn-TiO<sub>2</sub> photocatalyst**

591 Scheme 2 shows the proposed mechanism. Mn has modified the photoelectric  
592 properties of TiO<sub>2</sub> by producing an intermediate Mn *3d-O 2p* energy level within its  
593 energy gap. Above the valence band edge in Mn-TiO<sub>2</sub>, an intermediate energy level  
594 improves the separation of (e<sup>-</sup>/h<sup>+</sup>) pairs to facilitate the electron transfer and narrows  
595 the optical band gap to absorb more light by shifting the spectral photoresponse  
596 toward longer wavelengths. The half-filled electronic structure of Mn<sup>2+</sup> enhances the  
597 photocatalytic activity because of its electronic configuration *3d<sup>5</sup>*, which changes to *d<sup>4</sup>*  
598 when accepting h<sup>+</sup> and to *d<sup>6</sup>* upon receiving electrons (Y. Liu et al., 2020). The energy

599 level of the couple  $\text{Mn}^{2+}/\text{Mn}^+$  is below the conduction band edge, while that of  
600  $\text{Mn}^{2+}/\text{Mn}^{3+}$  is above the valence band of  $\text{TiO}_2$  (Zhang et al., 2012). Consequently,  
601  $\text{Mn(II)}$  can trap both  $\text{h}^+$  and electrons to assist the charge transfer process in  $\text{TiO}_2$   
602 (Eqs. (10) -(12)).  $\text{Mn(III)}$  is formed by oxidation of  $\text{Mn(II)}$  by  $\text{h}^+$  through a valence  
603 band process, and then free hydroxyl  $\text{OH}^-$  is quickly adsorbed and reacts with unstable  
604  $\text{Mn(III)}$  to produce adsorbed  $\bullet\text{OH}$  (Eq. (13)), which confirms that  $\bullet\text{OH}$  plays the main  
605 role in the AMB degradation, a result in agreement with the effect of ethanol. These  
606 reactions contribute to the charge's separation, which improves the photocatalytic  
607 efficiency according to the following sequences:



616

#### 617 **4. Conclusion**

618 In this work, a complete investigation was carried out for the characterization  
619 of  $\text{Mn-TiO}_2$  and its application for the photodegradation of AMB, which has not been  
620 studied before. The optimization of parameters affecting the photodegradation process  
621 was conducted and the radicals, photoproducts, mineralization and stability of the  
622 material were evaluated. We have demonstrated that  $\text{Mn-TiO}_2$  displayed a good  
623 photocatalytic activity and structural stability. The morphology, structural and optical

624 properties of the Mn-TiO<sub>2</sub> nanocomposite were investigated. The optimal parameters  
625 of the initial AMB concentration, Mn-TiO<sub>2</sub> dose and pH assessed by the response  
626 surface methodology and contour plots were 0.625 g.L<sup>-1</sup>, 30 ppm, and 7 respectively.  
627 At these optimal parameters, a complete photodegradation was achieved after 30 min  
628 of irradiation. The degradation kinetic obeyed a pseudo-first-order model. A high  
629 determination coefficient ( $R^2 = 0.998$  and  $\text{Adj-}R^2 = 0.996$ ) was obtained by the  
630 variance analysis, thus ensuring a satisfactory adjustment of the second-order  
631 regression model with the experimental results. Trapping experiments have  
632 demonstrated that hydroxyl radicals were the main active oxidant species. The  
633 UHPLC-ESI-HRMS and ionic chromatography techniques showed that the  
634 photocatalytic process could be used for a complete mineralization. Finally, the  
635 reusability of the photocatalyst for 4 consecutive cycles was shown. Such results  
636 provided proof of the high photocatalytic performance and chemical stability of Mn-  
637 TiO<sub>2</sub> which is also attractive from an economic point of view. Studies on other hetero-  
638 junctions or even other catalysts based on this material are in progress, and many  
639 applications are being targeted in addition to those in pollutant elimination (e.g.,  
640 antibacterial activity and H<sub>2</sub> production and storage).

641

642 **Acknowledgments:** A.T. thanks the Franco-Algerien “PROFAS B+” program for  
643 having granted her stay in the ICCF. The authors also thank Martin Leremboire  
644 (Engineer CNRS) and Frederic Emmenegger (Tech CNRS) for the UHPLC-HRMS  
645 analyses, Guillaume Voyard (Engineer CNRS) for assistance in the HPLC and ionic  
646 chromatography analyses, Claire Szczepaniak (UCA) for the MET analyses and  
647 Emmy Voyer (Tech, UCA) for the MEB analyses.

648

649 **References**

- 650 Abbas, M., Adil, M., Ehtisham-ul-Haque, S., Munir, B., Yameen, M., Ghaffar, A.,  
651 Shar, G.A., Asif Tahir, M., Iqbal, M., 2018. *Vibrio fischeri* bioluminescence  
652 inhibition assay for ecotoxicity assessment: A review. *Sci. Total Environ.* 626,  
653 1295–1309. <https://doi.org/10.1016/j.scitotenv.2018.01.066>
- 654 Ahmed, S.A., 2016. Annealing effects on structure and magnetic properties of Mn-  
655 doped TiO<sub>2</sub>. *J. Magn. Magn. Mater.* 402, 178–183.  
656 <https://doi.org/10.1016/j.jmmm.2015.11.065>
- 657 Amine-Khodja, A., Boulkamh, A., Richard, C., 2005. Phototransformaion of  
658 metobromuron in the presence of TiO<sub>2</sub>. *Appl. Cat. B: Environ.* 59, 147-154.  
659 <https://doi.org/10.1016/j.ap catb.2005.01.010>
- 660 Arshad, R., Bokhari, T.H., Javed, T., Bhatti, I.A., Rasheed, S., Iqbal, M., Nazir, A.,  
661 Naz, S., Khan, M.I., Khosa, M.K.K., Iqbal, M., Zia-Ur-Rehman, M., 2020.  
662 Degradation product distribution of Reactive Red-147 dye treated by  
663 UV/H<sub>2</sub>O<sub>2</sub>/TiO<sub>2</sub> advanced oxidation process. *J. Mater. Res. Technol.* 9, 3168–  
664 3178. <https://doi.org/10.1016/j.jmrt.2020.01.062>
- 665 Bagheri, N., Mansour Lakouraj, M., Hasantabar, V., Mohseni, M., 2021.  
666 Biodegradable macro-porous CMC-polyaniline hydrogel: synthesis,  
667 characterization and study of microbial elimination and sorption capacity of dyes  
668 from waste water. *J. Hazard. Mater.* 403, 123631.  
669 <https://doi.org/10.1016/j.jhazmat.2020.123631>
- 670 Bansal, P., Sud, D., 2013. Photocatalytic degradation of commercial dye, CI Reactive  
671 Red 35 in aqueous suspension: Degradation pathway and identification of  
672 intermediates by LC/MS. *J. Mol. Catal. A Chem.* 374–375, 66–72.  
673 <https://doi.org/10.1016/j.molcata.2013.03.018>

674 Beckers, L.M., Busch, W., Krauss, M., Schulze, T., Brack, W., 2018. Characterization  
675 and risk assessment of seasonal and weather dynamics in organic pollutant  
676 mixtures from discharge of a separate sewer system. *Water Res.* 135, 122–133.  
677 <https://doi.org/10.1016/j.watres.2018.02.002>

678 Bekkouche, S., Baup, S., Bouhelassa, M., Molina-Boisseau, S., Petrier, C., 2012.  
679 Competitive adsorption of phenol and heavy metal ions onto titanium dioxide  
680 (Dugussa P25). *Desalin. Water Treat.* 37, 364–372.  
681 <https://doi.org/10.1080/19443994.2012.661293>

682 Belabed, C., Haine, N., Benabdelghani, Z., Bellal, B., Trari, M., 2014. Photocatalytic  
683 hydrogen evolution on the hetero-system polypyrrol/TiO<sub>2</sub> under visible light.  
684 *Int. J. Hydrogen Energy* 39, 17533–17539.

685 Brüggemann, H., Köser, H., Meyer, E., Nguyen, T.H., 2003. Sonolytic debromination  
686 of ambroxol process wastewater. *Water Res.* 37, 674–680.  
687 [https://doi.org/10.1016/S0043-1354\(02\)00363-9](https://doi.org/10.1016/S0043-1354(02)00363-9)

688 Carvalho, K.T.G., Lopes, O.F., Ferreira, D.C., Ribeiro, C., 2019. ZnO:ZnWO<sub>4</sub>  
689 heterostructure with enhanced photocatalytic activity for pollutant degradation in  
690 liquid and gas phases. *J. Alloys Compd.* 797, 1299–1309.  
691 <https://doi.org/10.1016/j.jallcom.2019.05.144>

692 Das, D., Makal, P., 2020. Narrow band gap reduced TiO<sub>2</sub>-B:Cu nanowire  
693 heterostructures for efficient visible light absorption, charge separation and  
694 photocatalytic degradation. *Appl. Surf. Sci.* 506.  
695 <https://doi.org/10.1016/j.apsusc.2019.144880>

696 Dong, Z., Ding, D., Li, T., Ning, C., 2018. Ni-doped TiO<sub>2</sub> nanotubes photoanode for  
697 enhanced photoelectrochemical water splitting. *Appl. Surf. Sci.* 443, 321–328.  
698 <https://doi.org/10.1016/j.apsusc.2018.03.031>

699 Erady, V., Mascarenhas, R.J., Satpati, A.K., Bhakta, A.K., Mekhalif, Z., Delhalle, J.,  
700 Dhasan, A., 2019. Carbon paste modified with Bi decorated multi-walled carbon  
701 nanotubes and CTAB as a sensitive voltammetric sensor for the detection of  
702 Caffeic acid. *Microchem. J.* 146, 73–82.  
703 <https://doi.org/10.1016/j.microc.2018.12.023>

704 Fonseca, A.S., Viitanen, A.K., Kanerva, T., Säämänen, A., Aguerre-Chariol, O.,  
705 Fable, S., Dermigny, A., Karoski, N., Fraboulet, I., Koponen, I.K., Delpivo, C.,  
706 Villalba, A.V., Vázquez-Campos, S., Østerskov Jensen, A.C., Nielsen, S.H.,  
707 Sahlgren, N., Clausen, P.A., Nguyen Larsen, B.X., Kofoed-Sørensen, V., Jensen,  
708 K.A., Koivisto, J., 2021. Occupational exposure and environmental release: The  
709 case study of pouring TiO<sub>2</sub> and filler materials for paint production. *Int. J.*  
710 *Environ. Res. Public Health* 18, 1–26. <https://doi.org/10.3390/ijerph18020418>

711 Ganzenko, O., Trelu, C., Oturan, N., Huguenot, D., Péchaud, Y., van Hullebusch,  
712 E.D., Oturan, M.A., 2020. Electro-Fenton treatment of a complex pharmaceutical  
713 mixture: Mineralization efficiency and biodegradability enhancement.  
714 *Chemosphere* 253. <https://doi.org/10.1016/j.chemosphere.2020.126659>

715 Ghenaatgar, A., M.A.Tehrani, R., Khadir, A., 2019. Photocatalytic degradation and  
716 mineralization of dexamethasone using WO<sub>3</sub> and ZrO<sub>2</sub> nanoparticles:  
717 Optimization of operational parameters and kinetic studies. *J. Water Process*  
718 *Eng.* 32, 100969. <https://doi.org/10.1016/j.jwpe.2019.100969>

719 Ghosh, M., Manoli, K., Shen, X., Wang, J., Ray, A.K., 2019. Solar photocatalytic  
720 degradation of caffeine with titanium dioxide and zinc oxide nanoparticles. *J.*  
721 *Photochem. Photobiol. A Chem.* 377, 1–7.  
722 <https://doi.org/10.1016/j.jphotochem.2019.03.029>

723 Gu, S., Xia, M., Zhou, C., Kong, Z., Molokeyev, M.S., Liu, L., Wong, W.Y., Zhou, Z.,

724 2020. intermediate bands intermediate bands. Chem. Eng. J. 396, 125208.  
725 <https://doi.org/10.1016/j.cej.2020.125208>

726 Güy, N., Özacar, M., 2016. The influence of noble metals on photocatalytic activity of  
727 ZnO for Congo red degradation. Int. J. Hydrogen Energy 41, 20100–20112.  
728 <https://doi.org/10.1016/j.ijhydene.2016.07.063>

729 Iqbal, M., 2016. Vicia faba bioassay for environmental toxicity monitoring: A review.  
730 Chemosphere 144, 785–802. <https://doi.org/10.1016/j.chemosphere.2015.09.048>

731 Khan, J.A., Sayed, M., Shah, N.S., Khan, S., Zhang, Y., Boczkaj, G., Khan, H.M.,  
732 Dionysiou, D.D., 2020. Synthesis of eosin modified TiO<sub>2</sub> film with co-exposed  
733 {001} and {101} facets for photocatalytic degradation of para-aminobenzoic  
734 acid and solar H<sub>2</sub> production. Appl. Catal. B Environ. 265.  
735 <https://doi.org/10.1016/j.apcatb.2019.118557>

736 Li, N., Li, Y., Zhou, Y., Li, W., Ji, S., Yao, H., Cao, X., Jin, P., 2017. Interfacial-  
737 charge-transfer-induced photochromism of MoO<sub>3</sub>@TiO<sub>2</sub> crystalline-core  
738 amorphous-shell nanorods. Sol. Energy Mater. Sol. Cells 160, 116–125.  
739 <https://doi.org/10.1016/j.solmat.2016.10.016>

740 Li, W., Chen, C., Zhu, J., Zhou, L., Lan, Y., 2019. Efficient removal of aniline by  
741 micro-scale zinc-copper (mZn/Cu) bimetallic particles in acidic solution: An  
742 oxidation degradation mechanism via radicals, Journal of Hazardous Materials.  
743 Elsevier B.V. <https://doi.org/10.1016/j.jhazmat.2018.12.027>

744 Liu, B., Chen, H.M., Liu, C., Andrews, S.C., Hahn, C., Yang, P., 2013. Large-scale  
745 synthesis of transition-metal-doped TiO<sub>2</sub> nanowires with controllable  
746 overpotential. J. Am. Chem. Soc. 135, 9995–9998.  
747 <https://doi.org/10.1021/ja403761s>

748 Liu, H.Y., Yang, C.L., Wang, M.S., Ma, X.G., 2020. Two-dimensional

749 hexaphosphate BiMP6 (M = Al, Ga, In) with desirable band gaps and ultrahigh  
750 carrier mobility for photocatalytic hydrogen evolution. *Appl. Surf. Sci.* 517,  
751 146166. <https://doi.org/10.1016/j.apsusc.2020.146166>

752 Liu, J., Williams, P.C., Goodson, B.M., Geisler-Lee, J., Fakharifar, M., Gemeinhardt,  
753 M.E., 2019. TiO<sub>2</sub> nanoparticles in irrigation water mitigate impacts of aged Ag  
754 nanoparticles on soil microorganisms, *Arabidopsis thaliana* plants, and *Eisenia*  
755 *fetida* earthworms. *Environ. Res.* 172, 202–215.  
756 <https://doi.org/10.1016/j.envres.2019.02.010>

757 Liu, Y., Li, Y., Lin, Y., Yang, S., Zhang, Q., Peng, F., 2020. Theoretical calculations  
758 and controllable synthesis of MoSe<sub>2</sub>/CdS-CdSe with highly active sites for  
759 photocatalytic hydrogen evolution. *Chem. Eng. J.* 383, 123133.  
760 <https://doi.org/10.1016/j.cej.2019.123133>

761 Liu, Y., Zhu, Yanyan, Xu, J., Bai, X., Zong, R., Zhu, Yongfa, 2013. Degradation and  
762 mineralization mechanism of phenol by BiPO<sub>4</sub> photocatalysis assisted with  
763 H<sub>2</sub>O<sub>2</sub>. *Appl. Catal. B Environ.* 142–143, 561–567.  
764 <https://doi.org/10.1016/j.apcatb.2013.05.049>

765 Malakootian, M., Nasiri, A., Amiri Gharaghani, M., 2020. Photocatalytic degradation  
766 of ciprofloxacin antibiotic by TiO<sub>2</sub> nanoparticles immobilized on a glass plate.  
767 *Chem. Eng. Commun.* 207, 56–72.  
768 <https://doi.org/10.1080/00986445.2019.1573168>

769 Molnárová, O., Šittner, P., Veselý, J., Cieslar, M., 2020. TEM analysis of deformation  
770 bands created by tensile deformation of superelastic NiTi wires. *Mater. Charact.*  
771 167. <https://doi.org/10.1016/j.matchar.2020.110470>

772 Mona, S., Kaushik, A., Kaushik, C.P., 2011. Waste biomass of *Nostoc linckia* as  
773 adsorbent of crystal violet dye: Optimization based on statistical model. *Int.*

774 Biodeterior. Biodegrad. 65, 513–521. <https://doi.org/10.1016/j.ibiod.2011.02.002>

775 Moztahida, M., Lee, D.S., 2020. Photocatalytic degradation of methylene blue with  
776 P25/graphene/polyacrylamide hydrogels: Optimization using response surface  
777 methodology. *J. Hazard. Mater.* 400, 123314.  
778 <https://doi.org/10.1016/j.jhazmat.2020.123314>

779 Ning, X., Wang, X., Yu, X., Li, J., Zhao, J., 2016. Preparation and capacitance  
780 properties of Mn-doped TiO<sub>2</sub> nanotube arrays by anodisation of Ti-Mn alloy. *J.*  
781 *Alloys Compd.* 658, 177–182. <https://doi.org/10.1016/j.jallcom.2015.10.204>

782 Ong, C.B., Ng, L.Y., Mohammad, A.W., 2018. A review of ZnO nanoparticles as  
783 solar photocatalysts: Synthesis, mechanisms and applications. *Renew. Sustain.*  
784 *Energy Rev.* 81, 536–551. <https://doi.org/10.1016/j.rser.2017.08.020>

785 Oseghe, E.O., Ndungu, P.G., Jonnalagadda, S.B., 2015. Synthesis of mesoporous  
786 Mn/TiO<sub>2</sub> nanocomposites and investigating the photocatalytic properties in  
787 aqueous systems. *Environ. Sci. Pollut. Res.* 22, 211–222.  
788 <https://doi.org/10.1007/s11356-014-3356-z>

789 Pal, B., Kaur, R., Grover, I.S., 2016. Superior adsorption and photodegradation of  
790 eriochrome black-T dye by Fe<sup>3+</sup> and Pt<sup>4+</sup> impregnated TiO<sub>2</sub> nanostructures of  
791 different shapes. *J. Ind. Eng. Chem.* 33, 178–184.  
792 <https://doi.org/10.1016/j.jiec.2015.09.033>

793 Park, E., Le, H., Chin, S., Kim, J., Bae, G.N., Jurng, J., 2012. Synthesis and enhanced  
794 photocatalytic activity of Mn/TiO<sub>2</sub> mesoporous materials using the impregnation  
795 method through CVC process. *J. Porous Mater.* 19, 877–881.  
796 <https://doi.org/10.1007/s10934-011-9543-0>

797 Prashad Ojha, D., Babu Poudel, M., Joo Kim, H., 2020. Investigation of  
798 electrochemical performance of a high surface area mesoporous Mn doped TiO<sub>2</sub>

799 nanoparticle for a supercapacitor. *Mater. Lett.* 264, 127363.  
800 <https://doi.org/10.1016/j.matlet.2020.127363>

801 Qian, Y., Du, J., Kang, D.J., 2019. Enhanced electrochemical performance of porous  
802 Co-doped TiO<sub>2</sub> nanomaterials prepared by a solvothermal method. *Microporous*  
803 *Mesoporous Mater.* 273, 148–155.  
804 <https://doi.org/10.1016/j.micromeso.2018.06.056>

805 Ray, S., Lalman, J.A., Biswas, N., 2009. Using the Box-Benken technique to  
806 statistically model phenol photocatalytic degradation by titanium dioxide  
807 nanoparticles. *Chem. Eng. J.* 150, 15–24.  
808 <https://doi.org/10.1016/j.cej.2008.11.039>

809 Rossi, G., Pasquini, L., Catone, D., Piccioni, A., Patelli, N., Paladini, A., Molinari, A.,  
810 Caramori, S., O’Keeffe, P., Boscherini, F., 2018. Charge carrier dynamics and  
811 visible light photocatalysis in vanadium-doped TiO<sub>2</sub> nanoparticles. *Appl. Catal.*  
812 *B Environ.* 237, 603–612. <https://doi.org/10.1016/j.apcatb.2018.06.011>

813 Salazar, H., Martins, P.M., Santos, B., Fernandes, M.M., Reizabal, A., Sebastián, V.,  
814 Botelho, G., Tavares, C.J., Vilas-Vilela, J.L., Lanceros-Mendez, S., 2020a.  
815 Photocatalytic and antimicrobial multifunctional nanocomposite membranes for  
816 emerging pollutants water treatment applications. *Chemosphere* 250.  
817 <https://doi.org/10.1016/j.chemosphere.2020.126299>

818 Salazar, H., Martins, P.M., Santos, B., Fernandes, M.M., Reizabal, A., Sebastián, V.,  
819 Botelho, G., Tavares, C.J., Vilas-Vilela, J.L., Lanceros-Mendez, S., 2020b.  
820 Photocatalytic and antimicrobial multifunctional nanocomposite membranes for  
821 emerging pollutants water treatment applications. *Chemosphere* 250, 126299.  
822 <https://doi.org/10.1016/j.chemosphere.2020.126299>

823 Santara, B., Imakita, K., Fujii, M., Giri, P.K., 2016. Mechanism of defect induced

824 ferromagnetism in undoped and Cr doped TiO<sub>2</sub> nanorods/nanoribbons. *J. Alloys*  
825 *Compd.* 661, 331–344. <https://doi.org/10.1016/j.jallcom.2015.11.066>

826 Soji, D., Despotovi, V., Pazzi, M., Csanádi, J., 2011. *Applied Catalysis B :*  
827 *Environmental A* comparative study of the activity of TiO<sub>2</sub> Wackherr and  
828 Degussa P25 in the photocatalytic degradation of picloram  $\times 10^5$ , 191–198.  
829 <https://doi.org/10.1016/j.apcatb.2011.04.014>

830 Sousa, J.C.G., Ribeiro, A.R., Barbosa, M.O., Pereira, M.F.R., Silva, A.M.T., 2018. A  
831 review on environmental monitoring of water organic pollutants identified by EU  
832 guidelines. *J. Hazard. Mater.* 344, 146–162.  
833 <https://doi.org/10.1016/j.jhazmat.2017.09.058>

834 Tab, A., Dahmane, M., Chemseddin, B., Bellal, B., Trari, M., Richard, C., 2020.  
835 Photocatalytic degradation of quinoline yellow over Ag<sub>3</sub>PO<sub>4</sub>. *Catalysts* 10, 1–  
836 15. <https://doi.org/10.3390/catal10121461>

837 Tobajas, M., Belver, C., Rodriguez, J.J., 2017a. Degradation of emerging pollutants in  
838 water under solar irradiation using novel TiO<sub>2</sub>-ZnO/clay nanoarchitectures.  
839 *Chem. Eng. J.* 309, 596–606. <https://doi.org/10.1016/j.cej.2016.10.002>

840 Tobajas, M., Belver, C., Rodriguez, J.J., 2017b. Degradation of emerging pollutants in  
841 water under solar irradiation using novel TiO<sub>2</sub>-ZnO/clay nanoarchitectures.  
842 *Chem. Eng. J.* 309, 596–606. <https://doi.org/10.1016/j.cej.2016.10.002>

843 Vione, D., Minero, C., Maurino, V., Carlotti, M.E., Picatonotto, T., Pelizzetti, E.,  
844 2005. Degradation of phenol and benzoic acid in the presence of a TiO<sub>2</sub> -based  
845 heterogeneous photocatalyst 58, 79–88.  
846 <https://doi.org/10.1016/j.apcatb.2004.11.018>

847 Wang, M.C., Lin, H.J., Yang, T.S., 2009. Characteristics and optical properties of iron  
848 ion (Fe<sup>3+</sup>)-doped titanium oxide thin films prepared by a sol-gel spin coating. *J.*

849 Alloys Compd. 473, 394–400. <https://doi.org/10.1016/j.jallcom.2008.05.105>

850 Xu, B., Ahmed, M.B., Zhou, J.L., Altaee, A., 2020. Visible and UV photocatalysis of  
851 aqueous perfluorooctanoic acid by TiO<sub>2</sub> and peroxymonosulfate: Process kinetics  
852 and mechanistic insights. *Chemosphere* 243, 125366.  
853 <https://doi.org/10.1016/j.chemosphere.2019.125366>

854 Xu, J., Meng, W., Zhang, Y., Li, L., Guo, C., 2011. Photocatalytic degradation of  
855 tetrabromobisphenol A by mesoporous BiOBr: Efficacy, products and pathway.  
856 *Appl. Catal. B Environ.* 107, 355–362.  
857 <https://doi.org/10.1016/j.apcatb.2011.07.036>

858 Xu, J.H., Ma, Y.Q., Wei, J.P., Li, F.M., Peng, X.H., 2015. New insights into  
859 bromination process: Effective preparation of Ambroxol. *Chem. Pap.* 69, 722–  
860 728. <https://doi.org/10.1515/chempap-2015-0077>

861 Yanalak, G., Sarılmaz, A., Karanfil, G., Aslan, E., Ozel, F., Hatay Patir, I., 2020.  
862 Enhanced photocatalytic hydrogen evolution from band-gap tunable Ag<sub>2</sub>S:X  
863 (X = Ni, Co, Zn, Mn) nanocrystals: Effect of transition metal ions. *J. Photochem.*  
864 *Photobiol. A Chem.* 394, 112462.  
865 <https://doi.org/10.1016/j.jphotochem.2020.112462>

866 Yang, C.N., Peng, W.Y., Lin, L.C., Tsai, T.H., 2021. Protein unbound  
867 pharmacokinetics of ambroxol in the blood and brains of rats and the interaction  
868 of ambroxol with *Polygala tenuifolia* by multiple microdialysis. *J.*  
869 *Ethnopharmacol.* 269, 113764. <https://doi.org/10.1016/j.jep.2020.113764>

870 Yang, Y.Y., Liu, W.R., Liu, Y.S., Zhao, J.L., Zhang, Q.Q., Zhang, M., Zhang, J.N.,  
871 Jiang, Y.X., Zhang, L.J., Ying, G.G., 2017. Suitability of pharmaceuticals and  
872 personal care products (PPCPs) and artificial sweeteners (ASs) as wastewater  
873 indicators in the Pearl River Delta, South China. *Sci. Total Environ.* 590–591,

874 611–619. <https://doi.org/10.1016/j.scitotenv.2017.03.001>

875 Zhang Junwei, J., Fu Dafang, D., Xu, Y., Liu, C., 2010. Optimization of parameters  
876 on photocatalytic degradation of chloramphenicol using TiO<sub>2</sub> as photocatalyst  
877 by response surface methodology. *J. Environ. Sci.* 22, 1281–1289.  
878 [https://doi.org/10.1016/S1001-0742\(09\)60251-5](https://doi.org/10.1016/S1001-0742(09)60251-5)

879 Zhang, X., Zhao, L., Fan, C., Liang, Z., Han, P., 2012. First-principles investigation  
880 of impurity concentration influence on bonding behavior, electronic structure and  
881 visible light absorption for Mn-doped BiOCl photocatalyst. *Phys. B Condens.*  
882 *Matter* 407, 4416–4424. <https://doi.org/10.1016/j.physb.2012.08.002>

883 Zhang, Y., Duan, L., Wang, B., Liu, C.S., Jia, Y., Zhai, N., Blaney, L., Yu, G., 2020.  
884 Efficient multiresidue determination method for 168 pharmaceuticals and  
885 metabolites: Optimization and application to raw wastewater, wastewater  
886 effluent, and surface water in Beijing, China. *Environ. Pollut.* 261, 114113.  
887 <https://doi.org/10.1016/j.envpol.2020.114113>

888 Zhu, B., Fan, C., Xu, C., Wang, L., Bi, C., Zhang, X., Fan, Y., 2021. Multi-responsive  
889 luminescent sensors of two water-stable polynuclear Cd organic frameworks:  
890 Synthesis, structures and sensing of tetracycline, Cr<sub>2</sub>O<sub>7</sub><sup>2-</sup> and Fe<sup>3+</sup> ions in water.  
891 *Microchem. J.* 162, 105880. <https://doi.org/10.1016/j.microc.2020.105880>

892